AIP | Journal of Applied Physics

Phase-control in two-dimensional phononic crystals

N. Swinteck, S. Bringuier, J.-F. Robillard, J. O. Vasseur, A. C. Hladky-Hennion et al.

Citation: J. Appl. Phys. **110**, 074507 (2011); doi: 10.1063/1.3641634
View online: http://dx.doi.org/10.1063/1.3641634
View Table of Contents: http://jap.aip.org/resource/1/JAPIAU/v110/i7
Published by the American Institute of Physics.

Phase-control in two-dimensional phononic crystals

N. Swinteck,[1,a)] S. Bringuier,[1] J.-F. Robillard,[2] J. O. Vasseur,[2] A. C. Hladky-Hennion,[2] K. Runge,[1] and P. A. Deymier[1]
[1]*Department of Materials Science and Engineering, University of Arizona, Tucson, Arizona 85721, USA*
[2]*Institut d'Electronique, de Micro-électronique et de Nanotechnologie, UMR CNRS 8520, Cité Scientifique, Villeneuve d'Ascq Cedex 59652, France*

(Received 21 April 2011; accepted 10 August 2011; published online 4 October 2011)

A theoretical model is developed to ascertain the necessary band structure and equi-frequency contour (EFC) features of two-dimensional phononic crystals (PCs) for the realization of phase control between propagating acoustic waves. Two different PCs, a square array of cylindrical polyvinylchloride inclusions in air and a triangular array of cylindrical steel inclusions in methanol, offer band structures and EFCs with highly dissimilar features. We demonstrate that PCs with EFCs showing non-collinear wave and group velocity vectors are ideal systems for controlling the phase between propagating acoustic waves. Finite-difference time-domain simulations are employed to validate theoretical models and demonstrate the control of phase between propagating acoustic waves in PC structures. © *2011 American Institute of Physics*. [doi:10.1063/1.3641634]

I. INTRODUCTION

The field of phononic crystals (PCs) and acoustic metamaterials emerged over the past two decades. These materials are composite structures designed to tailor phonon dispersion through Bragg scattering, other multiple scattering processes, or local resonances to achieve a range of spectral (ω-space) and wave vector (k-space) properties. Spectral properties result from band gaps in the transmission spectra for stopping phonons[1] or narrow passing bands for filtering.[2,3] Wave vector properties result from passing bands with unique refractive characteristics, for example, negative refraction or zero-angle refraction, and can lead to such functions as sub-wavelength imaging[4,5] or collimation.[6,7] Other functions, such as wave guiding and mode localization, have been demonstrated in defected phononic structures.[8] Acoustic rectification and tunable properties have also been demonstrated using non-linear effects or coupling phonons with other types of excitations, such as magnons.[9,10] Only recently has progress been made in the extension of properties of PCs beyond ω-k space and into the space of acoustic wave phase (φ-space). The concept of phase control between propagating waves in any PC can be realized through analysis of its band structure and equi-frequency contours (EFCs).[11] In this paper, we aim to reveal the dominant mechanisms behind the control of phase between propagating acoustic waves in two-dimensional PCs.

To start, we provide a full theoretical and computational analysis of the phase properties of a PC comprised of a square array of polyvinylchloride (PVC) cylinders embedded in a host matrix of air (PVC/air system). In a certain range of operating frequencies, this crystal shows passing bands with nearly square EFCs centered off the gamma point (the center of the irreducible Brillouin zone). This feature allows for the realization of non-collinear wave and group velocity vectors in the PC. Under this condition, propagating Bloch waves travel at different phase velocities along paths consistent with their refracted angles. Accordingly, the relative phase between waves traveling through slabs of the PC depends strongly on the incidence angle of the incoming waves as well as the PC thickness. This PC additionally exhibits wave collimation via near zero-angle refraction, due to the square-like shape of the EFCs in this frequency range. As a result, acoustic waves with different wave vectors can superpose in nearly the same volume of crystal. Phase manipulation of superposed waves can result in constructive or destructive interferences between non-collinear incident beams. Moreover, there exists operating frequencies for which the circular EFC in air is larger than the first Brillouin zone of the PC, permitting several Bloch modes to exit the crystal, leading to the phenomena of beam splitting.

Using the same theoretical guidelines to model phase properties of the PVC/air PC, we investigate a triangular array of steel cylinders embedded in a host matrix of methanol (steel/methanol system). This PC offers band structure and EFC features that are highly dissimilar from the PVC/air system. Specifically, this PC shows passing bands with circular EFCs centered on the gamma point. This EFC feature allows for the realization of group velocity vectors that are collinear and anti-parallel to the excited Bloch wave vectors. In comparing these two PCs in terms of their band structures, EFCs, and theoretical models for phase control, we highlight the prevailing features that allow for the control of phase between propagating acoustic waves in two-dimensional PCs. We show that when the group velocity and wave vector in the PC are collinear and anti-parallel, substantial shifts in the relative phase of propagating acoustic waves do not result on account of the fact that all Bloch modes propagate with the same phase velocity. On the contrary, PCs with non-collinear wave and group velocity vectors, such as the PVC/air system, are ideal systems for phase control because each excited Bloch mode has a unique phase velocity. Accordingly, substantial phase differences do amount between propagating acoustic waves.

[a)]Author to whom correspondence should be addressed. Electronic mail: swinteck@email.arizona.edu.

This paper is organized as follows. In Sec. II, we describe the PVC/air model as well as the numerical methods used to generate band structures and simulate wave propagation in inhomogeneous, periodic media. In Sec. III, we derive an analytical basis for phase-control in the PVC/air system. This model is based on EFCs generated by the plane-wave expansion (PWE) method and is built for describing the phase characteristics of acoustic waves in the PC. This model is tested and confirmed with finite-difference time-domain (FDTD) simulations of acoustic waves impinging upon the inhomogeneous structure. We demonstrate phase-control for a single incident wave and show, by only changing the PC thickness, that the relative phase between two impinging acoustic waves can be precisely modulated. In Sec. IV, the theoretical model detailing the phase properties of the PVC/air system is contrasted with a model for the steel/methanol system. Finally, Sec. V presents conclusions drawn from this study and outlines essential band structure and EFC characteristics for the realization of phase control in two-dimensional PCs.

II. PVC/AIR PC: MODEL AND NUMERICAL METHODS

We analyze the properties of an infinite, periodic PVC/air PC as well as the refractive and phase properties of a finite slab of this PC immersed in air.

The PC is comprised of a square array of PVC inclusions embedded in a host matrix of air. The spacing between the cylinders (lattice parameter) is $a = 27$ mm and the radius of the inclusions is $r = 12.9$ mm. The PVC/air system parameters are: $\rho_{PVC} = 1364$ kg/m^3, $c_{t,PVC} = 1000$ m/s, $c_{l,PVC} = 2230$ m/s, $\rho_{Air} = 1.3$ kg/m^3, $c_{t,Air} = 0$ m/s, and $c_{l,Air} = 340$ m/s (ρ is density, c_t is transverse speed of sound, and c_l is longitudinal speed of sound).

The band structure and EFCs for the infinite, periodic PC are generated by the PWE method.[12] This numerical scheme replaces the elastic wave equation with an eigenvalue problem by taking the Fourier expansion of the elastic displacement field (and of the physical parameters of the constituent materials) along reciprocal lattice vectors. The PVC cylinders are considered infinitely rigid and of infinite height. The assumption of rigidity simplifies the band structure calculation and is enabled by a large contrast in density and speed of sound between the solid inclusions and the matrix medium. The results gathered from this analysis are applicable to other solid/air PCs of the same filling fraction because, in reference to other solids, air has an extremely small value in characteristic acoustic impedance. Four hundred forty-one reciprocal space vectors were utilized to ensure convergence on the solution. It should be noted that Fig. 1(b) shows the band structure along the edges of irreducible Brillouin zone and Fig. 1(c) shows a contour map of the dispersion surface taken between frequency values 13.0 and 16.0 kHz. Our study, from here on, will utilize the EFC consistent with 13.5 kHz in Fig. 1(c). At this operating frequency, there exist a large number of Bloch waves with group velocities that coincide with small degrees of refraction, allowing phase control to occur between propagating waves within the nearly same volume of crystal.

The finite PVC/air system consists of a slab of the PC placed in a surrounding environment composed of air. A schematic of the simulation space is pictured in Fig. 1(a). In that illustration, we have two regions of interest for this study: the input side (region to the left of the PC) and the output side (region to the right of the PC). On the input side, the desired number of acoustic wave sources is placed. These sources can assume any incident angle to the PC face and be set with any relative phase difference, respectively, allowing for complete analysis of the PC wave vector space (k-space) and phase-space (φ-space). The output side is reserved for the detection of exiting acoustic signals. Here, measurements can be taken to ascertain changes in the relative phase of the input beams.

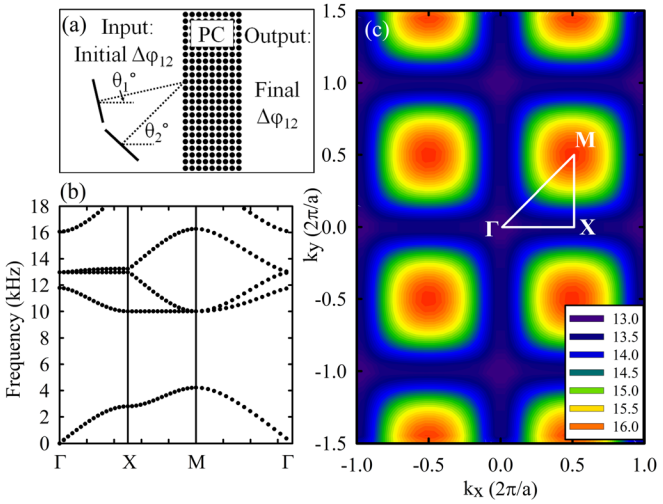

FIG. 1. (Color online) (a) Schematic illustration of two acoustic waves impinging upon the PC. The acoustic wave sources can assume any incident angle to the PC face and be set with any relative phase difference. (b) Band structure generated by PWE method along the edges of the irreducible Brillouin zone (pictured in (c)). (c) EFCs (extended zone scheme of irreducible Brillouin zone) in range of 13.0–16.0 kHz. The contour at 13.5 kHz is used throughout this study. At this frequency, there are several Bloch waves with group velocities that coincide with small degrees of refraction, allowing phase control to occur between propagating waves within the nearly same volume of crystal.

Simulations of acoustic waves impinging upon the finite PC are performed with the FDTD method.[13–17] In this method, the elastic wave equation is discretized in time and space on a square grid. For each source on the input side of the simulation space, we have a slanted line of grid points consistent with the desired incidence angle of the source. The nodes along this line are displaced in a direction orthogonal to the source line sinusoidally in time. At each time step, from spatial derivatives, the divergence of the stress tensor is calculated, which allows for the iterative update of the displacement field. Simulations are run for 2^{18} time steps with time step $dt = 7.92\ 10^{-8}$ seconds and $dx = dy = a/30$. These parameters are chosen to ensure convergence of the numerical method. To close the simulation space in the x and y directions, first order Mur absorbing boundary conditions are employed to avoid reflections and spurious simulation artifacts.[18]

III. PVC/AIR PC: ANALYTICAL MODEL AND FDTD VALIDATIONS

A. Phase shift for a single incident acoustic wave

The EFC corresponding to 13.5 kHz is shown in Fig. 2(a) along with the EFCs for 13.5 kHz acoustic waves in

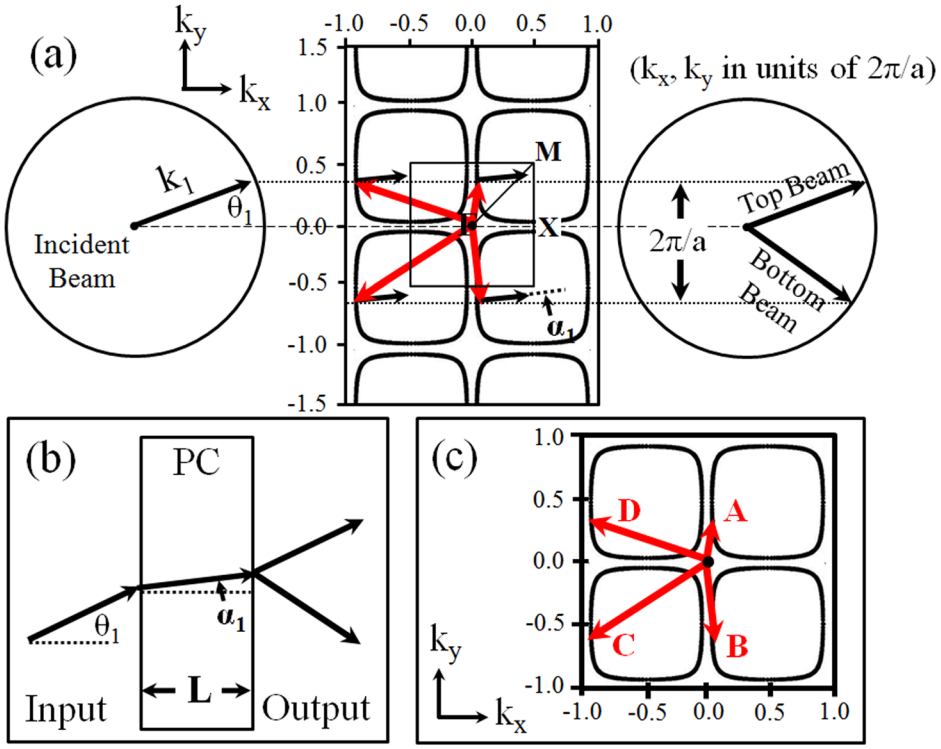

FIG. 2. (Color online) (a) Extended zone scheme representation of EFC of PC at 13.5 kHz (center) with the EFCs of 13.5 kHz acoustic waves in air (left and right circles). An incident acoustic wave impinges upon the PC face with incidence angle θ_1 and excites periodic Bloch modes throughout the k-space of the PC (arrows originating from the Gamma point). The group velocity vector is orthogonal to the dispersion surface and points in the direction of energy propagation. The parallel component of the Bloch waves is conserved at the interface between the PC and the exit medium, and two exiting modes are excited in air, leading to a split beam. (b) Schematic representation of the incident acoustic beam impinging upon the crystal. In the PC, the acoustic signal travels a path consistent with the angle of refraction. Upon exit from the crystal, we observe beam splitting. (c) Excited Bloch modes pictured in (a) with wave vectors $\overrightarrow{k_{1A}}$, $\overrightarrow{k_{1B}}$, $\overrightarrow{k_{1C}}$, and $\overrightarrow{k_{1D}}$.

air on the left- and right-hand sides. This diagram is particularly helpful for understanding wave propagation through PCs. An acoustic beam is directed at the PC face with incidence angle θ_1. The component of the input wave vector that is parallel to the surface of the PC is conserved at the interface, and periodic Bloch modes are excited in the k-space of the PC (wave vectors originating from the Gamma point in Fig. 2(a)). The direction of energy propagation is along the gradient to the dispersion surface (group velocity vector) and is not parallel to the k-vector of the Bloch waves. The incident wave propagates from the left of the crystal to the right along a path consistent with the angle of refraction (α_1). Only those Bloch waves inside the crystal that have a group velocity in that same direction will be excited. Positive refraction occurs at incident angles 2.3° to 28.1°, zero-angle refraction occurs at 28.1°, and negative refraction occurs at angles from 28.1° to 74.5°. Positive incidence angles below 2.3° or above 74.5° fall in the bandgap and will be totally reflected. By symmetry of reciprocal space, negative input angles in the range 2.3° to 28.1° and in the range 28.1° to 74.5° will negatively refract and positively refract, respectively. For input angles in the ranges 12° to 44° and –12° to –44°, the EFC has nearly flat faces and the incident beam will refract by less than 10°. These input angles are of interest for this study, because phase manipulation can occur within nearly the same volume of crystal. After propagation through the crystal, the parallel component of the excited Bloch waves is conserved at the interface between the PC and air. Because the EFC in air is larger than the PC's first Brillouin zone, multiple modes are excited in the exit medium and a split wave results. We draw attention to the fact that the exiting beams come from two different sets of wave vectors in the PC. The set of wave vectors that point down in Fig. 2(a) are linked to the exiting beam that travels downwards. The set of wave vectors that point up in Fig. 2(a) are linked to the exiting beam that travels upwards. All of these Bloch wave vectors have different magnitudes (different phase velocities) and can ultimately be traced back to a primary wave vector located within the first Brillouin zone by reciprocal lattice vector translations. We explore the consequence of waves of different phase velocities traveling the same path in the PC (along the path of the refracted beam) to understand the phase relationship between the top exit beam and bottom exit beam. For an arbitrary, incident input wave with wave vector $\overrightarrow{k_1}$, we describe the excited Bloch waves pictured in Fig. 2(a) with wave vectors $\overrightarrow{k_{1A}}$, $\overrightarrow{k_{1B}}$, $\overrightarrow{k_{1C}}$, and $\overrightarrow{k_{1D}}$ (Fig. 2(c)),

$$\overrightarrow{k_{1A}} = \frac{2\pi}{a}\{k_{1x}i + k_{1y}j\},$$

$$\overrightarrow{k_{1B}} = \frac{2\pi}{a}\{k_{1x}i + (k_{1y} - 1)j\},$$

$$\overrightarrow{k_{1C}} = \frac{2\pi}{a}\{(k_{1x} - 1)i + (k_{1y} - 1)j\},$$

$$\overrightarrow{k_{1D}} = \frac{2\pi}{a}\{(k_{1x} - 1)i + (k_{1y})j\},$$

where k_{1x} and k_{1y} are the components of the wave vector located in the first Brillouin zone (in units of $2\pi/a$) and i and j are unit vectors along axes k_x and k_y in Fig. 2(c), respectively. The path of the refracted beam in the PC is detailed as follows (an illustration is included in Fig. 2(b)):

$$\overrightarrow{r_1} = Li + Ltan(\alpha_1)j.$$

L is the thickness of the PC (distance from the entrance side of the crystal to the exit side: $L = na$, an integer number of lattice parameters) and α_1 is the angle the incident beam, $\overrightarrow{k_1}$,

is refracted by. Phase information for a plane wave with wave vector $\overrightarrow{k_{1A}}$ traveling a path consistent with $\overrightarrow{r_1}$ is detailed by Eq. (1),

$$\varphi_{1A} = \overrightarrow{k_{1A}} \cdot \overrightarrow{r_1} = \frac{2\pi L}{a}\{k_{1x} + tan(\alpha_1)k_{1y}\}. \quad (1)$$

Similarly, for Bloch modes with wave vectors $\overrightarrow{k_{1B}}$, $\overrightarrow{k_{1C}}$, and $\overrightarrow{k_{1D}}$ along the same path $\overrightarrow{r_1}$, we have

$$\varphi_{1B} = \overrightarrow{k_{1B}} \cdot \overrightarrow{r_1} = \frac{2\pi L}{a}\{k_{1x} + tan(\alpha_1)k_{1y} - tan(\alpha_1)\}, \quad (2)$$

$$\varphi_{1C} = \overrightarrow{k_{1C}} \cdot \overrightarrow{r_1} = \frac{2\pi L}{a}\{k_{1x} - 1 + tan(\alpha_1)k_{1y} - tan(\alpha_1)\}, \quad (3)$$

$$\varphi_{1D} = \overrightarrow{k_{1D}} \cdot \overrightarrow{r_1} = \frac{2\pi L}{a}\{k_{1x} - 1 + tan(\alpha_1)k_{1y}\}. \quad (4)$$

After propagation through the PC (along the path of the refracted beam), the phase-difference developed between two Bloch waves, for example, Bloch modes $\overrightarrow{k_{1A}}$ and $\overrightarrow{k_{1B}}$, is described by Eq. (5),

$$\varphi_{1A,1B} = \left(\overrightarrow{k_{1A}} - \overrightarrow{k_{1B}}\right) \cdot \overrightarrow{r_1} = \frac{2\pi L}{a}\{tan(\alpha_1)\} = 2\pi n\{tan(\alpha_1)\}. \quad (5)$$

The developed difference in phase between these modes is the tangent of the refracted angle (α_1) weighted by an integer multiple of 2π, where the integer (n) is the thickness of the PC in lattice parameters. For large values of α_1 or n, considerable phase differences between the modes result. For $\alpha_1 = 0°$ (zero-angle refraction), the phase-difference described with Eq. (5) becomes zero. This can be visualized in Fig. 2(a), for when $\alpha_1 = 0°$, the magnitudes of $\overrightarrow{k_{1A}}$ and $\overrightarrow{k_{1B}}$ are equal. Waves of the same phase velocity traveling the same path will not develop a lag in phase. Similarly, after propagation through the PC (along the path of the refracted beam), the phase-difference developed between Bloch modes with wave vectors, $\overrightarrow{k_{1A}}$ and $\overrightarrow{k_{1C}}$, is determined by Eq. (6),

$$\varphi_{1A,1C} = \left(\overrightarrow{k_{1A}} - \overrightarrow{k_{1C}}\right) \cdot \overrightarrow{r_1} = \frac{2\pi L}{a}\{1 + tan(\alpha_1)\} = 2\pi n + 2\pi n\{tan(\alpha_1)\}. \quad (6)$$

This result is equivalent to the result from Eq. (5) plus a factor of $2\pi n$. The additional term of $2\pi n$ is trivial when considering the relative phase between two beams: a $2\pi n$ translation added onto a particular phase-shift value of Φ provides no new information in terms of the relative phase between the two beams. Again, for large values of α_1 or n, large phase differences develop between propagating waves in the PC. Lastly, the phase-difference developed between Bloch waves with wave vectors $\overrightarrow{k_{1A}}$ and $\overrightarrow{k_{1D}}$ is

$$\varphi_{1A,1D} = \left(\overrightarrow{k_{1A}} - \overrightarrow{k_{1D}}\right) \cdot \overrightarrow{r_1} = \frac{2\pi L}{a} = 2\pi n. \quad (7)$$

Again, this term is trivial from the standpoint of measuring a relative phase shift between two beams. Ultimately, we arrive at the realization that $\overrightarrow{k_{1A}}$ and $\overrightarrow{k_{1B}}$ are sufficient for describing the relative phase between the top and bottom exit beams. Other pairs, such as $[\overrightarrow{k_{1A}}, \overrightarrow{k_{1C}}]$ or $[\overrightarrow{k_{1D}}, \overrightarrow{k_{1B}}]$ would result in the same relative phase difference seen between $\overrightarrow{k_{1A}}$ and $\overrightarrow{k_{1B}}$ with additional terms of $2\pi n$.

Each impinging acoustic beam to the PC is associated with a specific degree of refraction. The connection between the two is completely unique to the shape of the EFC. Figure 3(a) shows the connection between the incidence angle of an impinging acoustic wave (θ) and the angle at which that wave is refracted (α) for the 13.5 kHz EFC of the PVC/air system. We observe negative values for α at incidence angles greater than 28.1° and positive values for α at incidence angles smaller than 28.1°. This plot was generated with the raw data from the EFC in Fig. 2(a). Every impinging wave to the PC has a parallel wave vector component that coincides with a (k_x, k_y) coordinate value on the EFC (an excited Bloch mode). At this coordinate, a line is fit between it and its neighbors. A line perpendicular to this linear interpolation has a slope consistent with the angle of refraction for that Bloch mode. This process is carried out for several impinging acoustic beams with different incidence angles. In being able to link incidence angle (θ) to refracted angle (α), we plot the phase shift between the top exit beam and bottom exit beam (Eq. (5)) in Fig. 3(b). Here, we present results in terms of phase-shift per crystal thickness (L). This figure shows that the relative phase between the exiting beams is fully dependent upon the incidence angle of the impinging acoustic wave. To validate Eq. (5), we conducted a series of

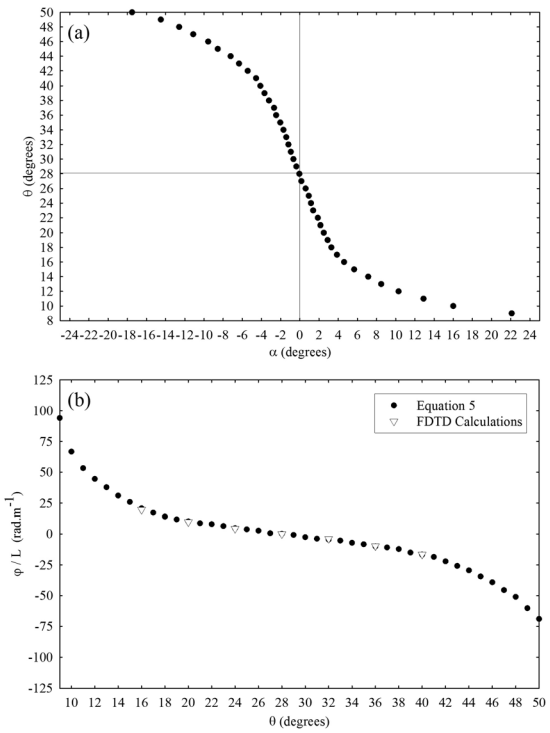

FIG. 3. (a) Relationship between incidence angle (θ) and refracted angle (α) for PVC/air PC at 13.5 kHz. (b) The phase difference per PC thickness (L) between the top and bottom exiting beams for a single acoustic wave input at a particular incidence angle. Selection of the acoustic beam incidence angle allows for control of the phase between exiting beams. Filled circles represent Eq. (5) and unfilled triangles represent FDTD calculations. A PC of $L = 20$ lattice parameters was used in FDTD validations.

FDTD simulations to measure the phase difference between the top and bottom exit beams. For these measurements, individual planes waves, each with a unique incidence angle, are directed at the PC face. On the exit side of the crystal, the displacement field in the path of the top exit beam and bottom exit beam is surveyed over time. Comparing the time evolution of the displacement field on the exit side of the PC from the top beam with that from the bottom beam allows us to quantify a phase-shift between the top and bottom exit beams for a given incident angle. The results from these calculations are included in Fig. 3(b). Despite using finite width beams in the FDTD simulations and not plane waves, the FDTD calculations correlate extremely well with Eq. (5). As a result, with the PVC/air PC, the relative phase between the split beams on the exit side of the crystal is entirely dependent upon the incident angle of the acoustic wave source.

B. Phase difference between two incident waves

The phase difference that develops between a pair of incident waves in the PC is of particular interest to this study. Two impinging waves with wave vectors $\overrightarrow{k_1}$ and $\overrightarrow{k_2}$ excite several Bloch modes throughout the k-space of the PC (Fig. 4(a)). From Subsection III A, for each incident wave vector, only two Bloch modes are necessary to describe the wave physics in this PC in terms of phase. Incident wave vector $\overrightarrow{k_1}$ excites Bloch modes $\overrightarrow{k_{1A}}$ and $\overrightarrow{k_{1B}}$ in the PC k-space (Fig. 4(a)) and coincides with a refracted angle of α_1. Incident wave vector $\overrightarrow{k_2}$ excites Bloch modes $\overrightarrow{k_{2A}}$ and $\overrightarrow{k_{2B}}$ (Fig. 4(a)) and coincides with a refracted angle of α_2. We could, of course, exhaustively evaluate the relative phase differences that result from the two beams traveling their respective paths of travel in the PC for any combination of $\overrightarrow{k_{1A}}$, $\overrightarrow{k_{1B}}$, $\overrightarrow{k_{2A}}$, and $\overrightarrow{k_{2B}}$; however, we rather consider only two possibilities: the phase difference between $\overrightarrow{k_{1A}}$ and $\overrightarrow{k_{2A}}$ ($\varphi_{1A,2A}$) and the phase difference between $\overrightarrow{k_{1B}}$ and $\overrightarrow{k_{2B}}$ ($\varphi_{1B,2B}$). $\overrightarrow{k_{1A}}$ and $\overrightarrow{k_{2A}}$ are the excited wave vectors in the PC that are linked to the exiting beams that travel upwards. $\overrightarrow{k_{1B}}$ and $\overrightarrow{k_{2B}}$ are the excited wave vectors in the PC that are linked to the downwards traveling exit beams. The upwards traveling exit beams intersect at a point on the exit side of the crystal, as do the downwards traveling exit beams (Fig. 4(b)). These points are valuable, because the relative phase between two beams can be ascertained at one location in space. It is for this reason that we consider $\varphi_{1A,2A}$ and $\varphi_{1B,2B}$.

The Bloch wave vectors in Fig. 4(a) are detailed as follows:

$$\overrightarrow{k_{1A}} = \frac{2\pi}{a}\{k_{1x}i + k_{1y}j\},$$

$$\overrightarrow{k_{1B}} = \frac{2\pi}{a}\{k_{1x}i + (k_{1y} - 1)j\},$$

$$\overrightarrow{k_{2A}} = \frac{2\pi}{a}\{k_{2x}i + k_{2y}j\},$$

$$\overrightarrow{k_{2B}} = \frac{2\pi}{a}\{k_{2x}i + (k_{2y} - 1)j\},$$

where k_{1x} and k_{1y} are the components of the wave vector $\overrightarrow{k_{1A}}$ and k_{2x} and k_{2y} are the components of the wave vector $\overrightarrow{k_{2A}}$ (in units of 2π/a). i and j are unit vectors along axes k_x and k_y in Fig. 4(a), respectively. The incident beam $\overrightarrow{k_1}$ is refracted by an angle α_1 and travels a path in the PC consistent with

$$\overrightarrow{r_1} = Li + Ltan(\alpha_1)j.$$

The incident beam $\overrightarrow{k_2}$ is refracted by an angle α_2 and travels a path that coincides with

$$\overrightarrow{r_2} = Li + Ltan(\alpha_2)j.$$

Equation (8) details phase information for a plane wave with wave vector $\overrightarrow{k_{1A}}$ traveling a path consistent with $\overrightarrow{r_1}$,

$$\varphi_{1A} = \overrightarrow{k_{1A}} \cdot \overrightarrow{r_1} = \frac{2\pi L}{a}\{k_{1x} + tan(\alpha_1)k_{1y}\}. \quad (8)$$

Similarly, for a wave vector $\overrightarrow{k_{1B}}$ in a direction $\overrightarrow{r_1}$, wave vector $\overrightarrow{k_{2A}}$ in a direction $\overrightarrow{r_2}$, and wave vector $\overrightarrow{k_{2B}}$ in a direction $\overrightarrow{r_2}$, we have Eqs. (9), (10), and (11), respectively,

$$\varphi_{1B} = \overrightarrow{k_{1B}} \cdot \overrightarrow{r_1} = \frac{2\pi L}{a}\{k_{1x} + tan(\alpha_1)k_{1y} - tan(\alpha_1)\}, \quad (9)$$

$$\varphi_{2A} = \overrightarrow{k_{2A}} \cdot \overrightarrow{r_2} = \frac{2\pi L}{a}\{k_{2x} + tan(\alpha_2)k_{2y}\}, \quad (10)$$

$$\varphi_{2B} = \overrightarrow{k_{2B}} \cdot \overrightarrow{r_2} = \frac{2\pi L}{a}\{k_{2x} + tan(\alpha_2)k_{2y} - tan(\alpha_2)\}. \quad (11)$$

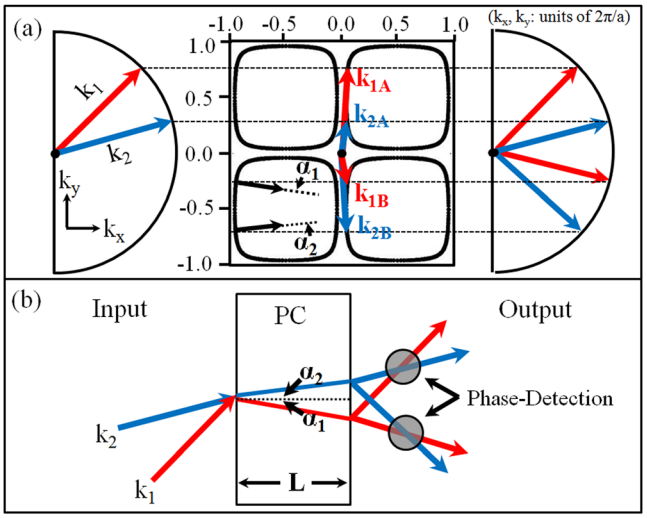

FIG. 4. (Color online) (a) EFC of PVC/air PC at 13.5 kHz (center) with two half circles (left and right) that represent the EFCs of 13.5 kHz acoustic waves in air. Two incident waves with wave vectors $\overrightarrow{k_1}$ and $\overrightarrow{k_2}$ are directed at the PC face. The impinging wave, $\overrightarrow{k_1}$, excites Bloch modes in the PC detailed with the arrows $\overrightarrow{k_{1A}}$ and $\overrightarrow{k_{1B}}$. The impinging wave, $\overrightarrow{k_2}$, excites Bloch modes in the PC, detailed with the arrows $\overrightarrow{k_{2A}}$ and $\overrightarrow{k_{2B}}$. $\overrightarrow{k_{1A}}$ and $\overrightarrow{k_{2A}}$ are the excited Bloch wave vectors in the PC that are linked to the exiting beams that travel upwards. $\overrightarrow{k_{1B}}$ and $\overrightarrow{k_{2B}}$ are the Bloch wave vectors that are linked to the downwards traveling exit beams. α_1 and α_2 are the respective angles of refraction for the impinging acoustic waves with wave vectors $\overrightarrow{k_1}$ and $\overrightarrow{k_2}$ (b) A schematic illustration of wave propagation described in (a). $\overrightarrow{k_1}$ is negatively refracted by α_1, and $\overrightarrow{k_2}$ is positively refracted by α_2. On the exit side of the crystal, there are four observed beams. The top exiting beams intersect at a location outside the PC, as do the bottom exiting beams. These points of intersection are used in FDTD simulations to ascertain relative phases between exiting beams. Negative branches in the PVC/air band structure must be utilized to observe exit beam intersection. If the gradient to the dispersion surface were not pointing to the inside of the EFC, the beams would diverge from each other in the PC and there would not be an intersection of beam paths on the exit side of the crystal.

After propagation through the PC, the developed phase difference between Bloch modes with wave vectors $\overrightarrow{k_{1A}}$ and $\overrightarrow{k_{2A}}$ is described with the difference between Eq. (8) and Eq. (10),

$$\varphi_{1A,2A} = \overrightarrow{k_{1A}} \cdot \overrightarrow{r_1} - \overrightarrow{k_{2A}} \cdot \overrightarrow{r_2},$$
$$\varphi_{1A,2A} = \frac{2\pi L}{a}\left\{k_{1x} + tan(\alpha_1)k_{1y} - k_{2x} - tan(\alpha_2)k_{2y}\right\}. \quad (12)$$

Equation (12) describes the relative phase shift developed between Bloch waves with wave vectors $\overrightarrow{k_{1A}}$ and $\overrightarrow{k_{2A}}$ strictly due to the PC thickness (L). This equation strictly applies to the upwards traveling exit beams. Similarly, the developed phase difference between Bloch modes with wave vectors $\overrightarrow{k_{1B}}$ and $\overrightarrow{k_{2B}}$ is described with the difference between Eq. (9) and Eq. (11),

$$\varphi_{1B,2B} = \overrightarrow{k_{1B}} \cdot \overrightarrow{r_1} - \overrightarrow{k_{2B}} \cdot \overrightarrow{r_2},$$
$$\varphi_{1B,2B} = \frac{2\pi L}{a}\{k_{1x} + tan(\alpha_1) \times (k_{1y} - 1) - k_{2x} - tan(\alpha_2)(k_{2y} - 1)\}. \quad (13)$$

Equation (13) describes the relative phase shift developed between Bloch waves with wave vectors $\overrightarrow{k_{1B}}$ and $\overrightarrow{k_{2B}}$ strictly due to the PC thickness (L). This equation strictly applies to the downwards traveling exit beams. Equations (12) and (13) are shown in Figs. 5(a) and 5(b), respectively. For these figures, we establish a reference state, where $\overrightarrow{k_2}$ is the wave vector describing an impinging acoustic wave with incidence angle equal to 28.1° (zero-angle refraction: $\alpha_2 = 0°$). The coordinate values, (k_{1x}, k_{1y}) and (k_{2x}, k_{2y}), used in Eq. (12) and Eq. (13) are extracted from the raw EFC data in Fig. 2(a) — the parallel component of every impinging wave vector associates with an excited Bloch mode (kx, ky) on the EFC.

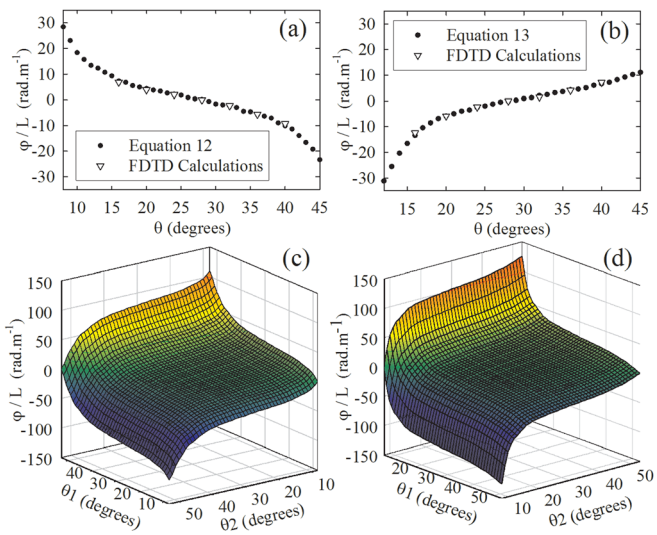

FIG. 5. (Color online) Two impinging acoustic beams to the PVC/air PC. (a) The developed difference in phase between a wave with incidence angle (θ) and a reference wave corresponding to zero-angle refraction (incident angle = 28.1°). The phase shift is strictly due to the PC thickness and describes the upwards traveling exit beams. (b) Same as (a), but for the downwards traveling exit beams. (c) The developed phase difference between two propagating waves with incidence angles θ_1 and θ_2 strictly due to the PC thickness (upwards traveling exit beams). (d) Same as (c), but for the downwards traveling exit beams.

Figures 5(a) and 5(b) show that the phase shift between the top exiting beams (Eq. (12)) and the bottom exiting beams (Eq. (13)) is attributed to two mechanisms: One, the paths of travel inside the PC for the propagating waves are different ($\overrightarrow{r_1} \neq \overrightarrow{r_2}$). Two, along these directions of propagation, the acoustic waves travel at different phase velocities ($|\overrightarrow{k_{1A}}| \neq |\overrightarrow{k_{2A}}|$ and $|\overrightarrow{k_{1B}}| \neq |\overrightarrow{k_{1B}}|$). Waves of different phase velocities traveling different paths certainly will develop a phase shift. In exploring Eq. (12) and Eq. (13), if the angle of refraction for all incident waves became zero (the EFC of the PC turns into a perfect square), then all the elements in the brackets with the tangent function would vanish and k_{1x} would equal k_{2x}. For this case, a zero phase shift would occur between all pairs of acoustic wave inputs. To observe a relative phase shift between a pair of acoustic beams in the PC, the angle of refraction associated with each incident beam to the crystal must be non-zero. We validate Eq. (12) and Eq. (13) with FDTD simulations. First, an impinging acoustic wave with incidence angle equal to 28.1° is directed at the PC face. On the exit side of the crystal in the path of the top exit beam and bottom exit beam, the displacement field is surveyed over time. These recordings represent our reference state for the top and bottom exit beams. Next, an impinging acoustic wave with incidence angle different from 28.1° is directed at the PC face. We again record the time evolution of the displacement field in the path of the top and bottom exit beams. Comparing the time evolution of the displacement field for the top and bottom exit beams for this particular angle with our reference data allows for the quantification of a phase-shift. This process is carried out for several incident angles different from 28.1°. In Figs. 5(a) and 5(b), the FDTD calculations correlate extremely well with the analytical model. We ultimately see that it is the incidence angles of the impinging wave vectors ($\overrightarrow{k_1}$ and $\overrightarrow{k_2}$) that determine (1) the phase velocities of the excited Bloch modes in the PC and (2) the angles of refraction. These factors entirely contribute to changes in phase between propagating waves. It is clear that incidence angle selection can be used to modulate the relative phase between propagating acoustic beams.

A space can be developed from Eq. (12) and Eq. (13). This is shown in Figs. 5(c) and 5(d). Any pair of incident waves to the crystal, for example, $\overrightarrow{k_1}$ at θ_1 and $\overrightarrow{k_2}$ at θ_2, will yield a particular value for a relative phase shift between them after traveling through the PC. One reads the plots as follows: after propagation through a crystal of thickness L, the phase-shift developed between the acoustic wave with incident angle θ_1 and the acoustic wave with incident angle θ_2 is the value in radians read from the z-axis (φ/L). These figures describe the phase shift developed between two incident beams, strictly due to the PC thickness. Figure 5(c) applies to the exiting beams that travel upwards and Fig. 5(d) applies to the exiting beams that travel downwards. A convenient and practical location on the backside of the crystal to measure the relative phase between the top exit beams and bottom exit beams is at the point where these beams intersect (Fig. 4(b)). With this convention, an additional component must be added on to the information contained within Figs. 5(c) and 5(d): the relative phase contribution coming from the point where the beams exit the crystal to the point where they intersect in air on the

output side of the PC. This component is merely a consideration of different path lengths in non-dispersive media. For each set of incident waves to the crystal, this additional phase value is determined from comparing path lengths calculated from the angles at which the top exit beams and bottom exit beams leave the PC and knowledge of where the beams exit the backside of the crystal. These additional calculations are added onto the information in Figs. 5(c) and 5(d). In Figs. 6(a)–(6d), we present plots for total phase shift. Total phase shift refers to the phase difference developed from the point where the beams first enter the crystal to the point where the beams intersect in air on the exit side of the PC. Figures 6(a) and 6(b) show the total phase shift between two incident beams with incidence angles θ_1 and θ_2 for crystals of thickness 23 lattice parameters and 46 lattice parameters, respectively (for the upwards traveling exit beams). Figures 6(c) and 6(d) show the total phase shift between two incident beams with incidence angles θ_1 and θ_2 for crystals of thickness 23 lattice parameters and 46 lattice parameters, respectively (for the downwards traveling exit beams). Crystal thicknesses of 23 and 46 lattice parameters are shown, because these L values are utilized in later FDTD validations.

In FDTD simulations, the initial relative phase between the input beams is determined at the point of beam entry into the PC (the center of the beams enter at precisely the same location). We survey a line of nodes at this intersection over one wave cycle and average the values for instantaneous pressure. This average represents a measurement that locally describes wave amplitudes. If the average value in instantaneous pressure over one wave cycle (average pressure) reads zero at the point of beam intersection, then destructive interference has occurred and the beams are π-radians out of phase. Conversely, if a maximum value reading is recorded at the point of beam intersection, then constructive interference has occurred and the beams are in-phase. The relative phase between the beams on the exit side of the crystal (at the point of beam intersection) is measured the same way. In having the initial relative phase between the beams and the final relative phase between the beams, we can ascertain the total relative phase shift initiated by the PVC/air system.

We show the ability of this system to modulate the relative phase between a pair of input acoustic beams. From Fig. 6(a) ($L=23$ lattice parameters), for $\theta_1=12°$ and $\theta_2=41°$, the total relative phase shift observed between the beams is approximately π radians. From Fig. 6(b) ($L=46$ lattice parameters), for input beams with the same incidence angles, the total relative phase shift observed between the beams is approximately 2π radians. Figure 7(a) shows the two sources impinging upon the thinner PC ($L=23$ lattice parameters). There are two black lines drawn in the simulation space. Average pressure readings are taken along these lines and are shown in Fig. 7(b). Figure 7(b) shows an interference pattern with characteristic central and peripheral lobes on the entrance side of the PC. The beams are initially in-phase because we observe a maximum value in average pressure in the middle of the cut. After propagating through the PC, the relative phase of the beams is altered by approximately π radians, because at the point of beam intersection on the exit side of the crystal, we observe a minimum at the center of

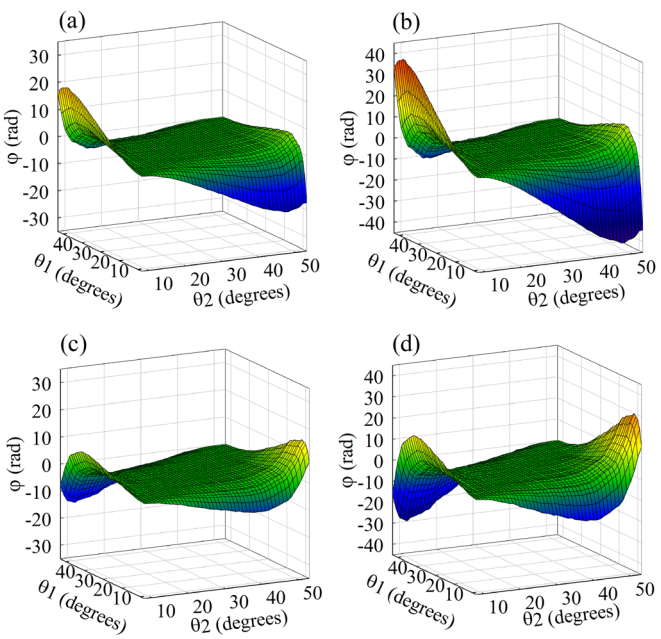

FIG. 6. (Color online) Total phase shift developed between two impinging acoustic beams at incidence angles (θ_1, θ_2) for: (a) the top exit beams with PC of thickness 23 lattice parameters, (b) the top exit beams with PC of thickness 46 lattice parameters, (c) the bottom exit beams with PC of thickness 23 lattice parameters, and (d) the bottom exit beams with PC of thickness 46 lattice parameters. Total phase shift refers to the phase difference developed from the point where the beams first enter the crystal to the point where the beams intersect on the exit side of the PC.

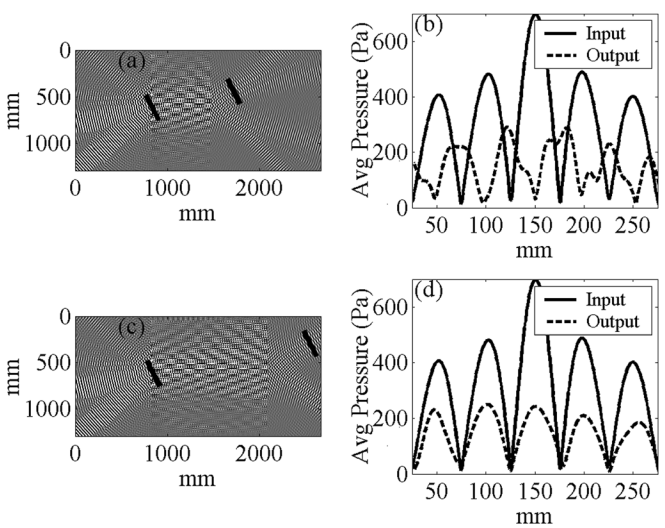

FIG. 7. (a) FDTD simulation (instantaneous pressure plot) showing two acoustic waves (at incidence angles $\theta_1=12°$ and $\theta_2=44°$) impinging upon a PC with $L=23$ lattice parameters. Average pressure measurements are taken along the black lines. (b) The average pressure readings along black lines in (a). The input cut shows a maximum in average pressure at its center — the beams are initially in phase. The output cut shows a minimum in average pressure at its center — the beams are out of phase. The total phase shift seen in (a) is π radians. (c) Same as (a), but $L=46$ lattice parameters. (d) The average pressure reading along black lines in (c). On the entrance side of the PC, we observe in-phase beams. On the exit side of the PC, this pattern is preserved. Average pressure maxima from the input side are aligned with average pressure maxima from the exit side. Constructive interferences account for this similarity, and a 2π radian phase shift has been measured.

the cut. Every maximum from the input average pressure cut matches up with a minimum from the average pressure cut taken on the backside of the crystal. Destructive interferences, indicative of a π phase shift, account for this contrast. The asymmetry in the output reading is due to mismatch loss at the entrance side of the PC. Figure 7(c) shows the two sources impinging upon the thicker PC ($L = 46$ lattice parameters). As before, the cut on the entrance side of the PC shows a characteristic interference pattern suggestive of in-phase beams. On the exit side of the PC (Fig. 7(d)), this pattern is preserved. Average pressure maxima from the input side are aligned with average pressure maxima from the exit side. Opposite to Fig. 7(b), constructive interferences account for this similarity. The total phase shift observed between the beams is approximately 2π radians. The relative phase between a pair of acoustic beams can be controlled by varying the crystal length or changing the incident angles of the acoustic beam sources.

C. Effect of phase shift on interference between complementary incident waves

Another feature of this PC comes from the fact that the EFC in air is larger than the first Brillouin zone. Acoustic wave inputs with different incident angles can excite the same Bloch waves in the PC. We call these acoustic wave pairs complementary angle inputs. Figures 8(a) and 8(b) show a pair of complementary angle inputs, incident angles 28.1° and –28.1°. In Fig. 8(a), these acoustic wave sources oscillate in-phase. In the crystal, along the paths of the refracted beams, there is constructive interference between the beams,

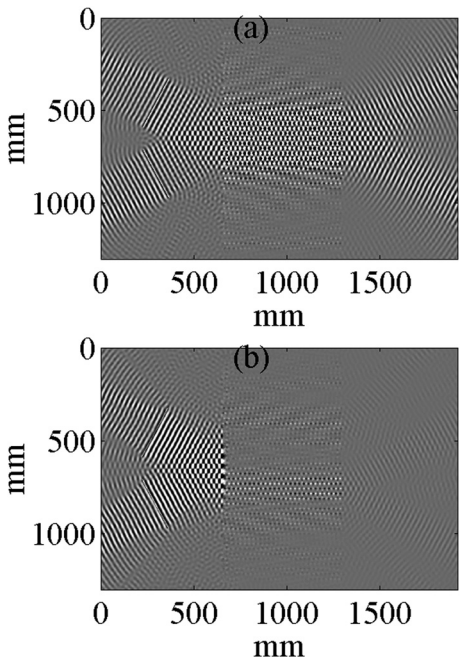

FIG. 8. (a) In-phase complementary angle inputs at 28.1° and –28.1°. There is constructive interference inside the PC along the path of the refracted beams, and two intense exit beams appear on the outside of the PC. (b) Out-of-phase complementary angle inputs at 28.1° and –28.1°. Due to this initial phase shift, amplitudes cancel along the path of the refracted beams and a minimal field of instantaneous pressure is shown on the outside of the PC.

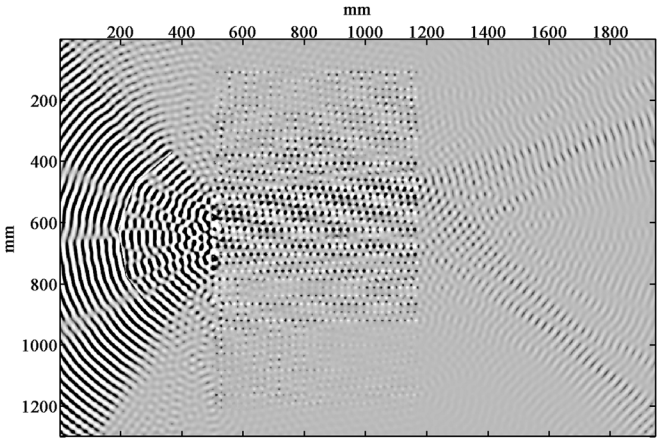

FIG. 9. Two pairs of complementary angle inputs are directed at the PC face. Impinging beams with incidence angles 10° and –50° excite the same Bloch waves in the PC as do impinging beams with incidence angles 38° and –19°. The source angled at 10° oscillates π radians out-of-phase with the source angled at –50°. The source angled at 38° oscillates π radians out-of-phase with the source angled at –19°. The initial phase relationship between these inputs ensures cancellation of amplitudes along the paths of the refracted input beams, and a minimal field of instantaneous pressure is shown on the outside of the PC.

and two intense exit beams appear on the backside of the crystal. If the sources are set to oscillate out-of-phase (Fig. 8(b)), there is cancellation of amplitudes inside the PC along the paths of the refracted beams. What appears on the exit side of the crystal in this instance is a very weak pressure field. These input waves coincide with zero-angle refraction, and perfect collimation is observed in the PC. The PVC/air system can support a large number of complementary angle inputs. For instance, observe Fig. 9. Two pairs of complementary angle inputs are directed at the PC face. Impinging beams with incidence angles 10° and –50° excite the same Bloch waves in the PC, as do impinging beams with incidence angles 38° and –19°. The source angled at 10° is set π radians out of phase, with the source angled at –50°. Similarly, the source angled at 38° is set π radians out of phase, with the source angled at –19°. The initial phase relationship between these inputs ensures cancellation of amplitudes along the paths of the refracted beams. In Fig. 9, on the exit side of the crystal, we observe a minimal reading in instantaneous pressure, indicative of complementary beam cancellation. Again, cancellation is not total due to mismatch loss at the entrance of the PC, which is dependent on the angle of incidence.

The PVC/air system possesses the ability to modulate the relative phase between a pair of acoustic waves. This function is enabled by having excited Bloch waves in the PC with different phase velocities that propagate along different paths. In particular, phase control in the PVC/air system arises from non-collinear wave and group velocity vectors in the PC.

IV. STEEL/METHANOL SYSTEM

We contrast the PVC/air system with a triangular array of steel cylinders embedded in a host matrix of methanol. This system allows for the realization of circular EFCs centered on the gamma point, whereas in the PVC/air system,

we observed square-like EFCs centered off the gamma point. In the steel/methanol scheme, in a certain range of operating frequencies, the group velocity vector and wave vector of the excited Bloch mode are always collinear, which implies that the phase velocity of all excited Bloch waves is identical. The consequence this feature has on the phase of propagating acoustic waves is explored in this section. For consistency, we take the same theoretical approach as was used in developing the PVC/air scheme. Specifically, we develop a scheme detailing the total phase shift between a pair of acoustic beams entering the steel/methanol system. Total phase shift refers to the phase difference developed from the point where the beams first enter the crystal to the point where the beams intersect on the exit side of the PC.

For the steel/methanol PC, a radius of $r = 0.51$ mm is used for the cylindrical steel inclusions and the lattice parameter is $a = 1.27$ mm. The system parameters are: $\rho_{steel} = 7890$ kg/m^3, $c_{t,steel} = 3100$ m/s, $c_{l,steel} = 5800$ m/s, $\rho_{methanol} = 0.790$ kg/m^3, $c_{t,methanol} = 0$ m/s, $c_{l,methanol} = 1138$ m/s (ρ is density, c_t is transverse speed of sound, and c_l is longitudinal speed of sound). The band structure for the infinite, periodic steel/methanol PC is generated by the FDTD technique.[19] The PWE method cannot be utilized in this instance, because one cannot assume infinite rigidity of the inclusion with a solid/fluid system — methanol has too large a value in characteristic acoustic impedance for the assumption of rigidity at the interface between the inclusion and matrix medium to be valid. The FDTD technique utilizes a square grid of mesh points with periodic boundary conditions to describe the repeatable unit cell for the PC structure. For a particular wave vector along the irreducible Brillouin zone, an initial delta function spike in the displacement field of the mesh perturbs the system. The time evolution of the displacement field for several, random grid points are recorded and, upon fast Fourier transform of this data set, the eigenfrequencies of the system can be resolved for the particular wave vector. The band structure along the ΓM direction in the *k*-space of the PC is pictured in Fig. 10. In the frequency range of 530–570 kHz, we observe a passing band with negative group velocity. Circular EFCs exist in this region where the group velocity vector and wave vector of the excited Bloch mode are collinear and anti-parallel.

If a slab of this PC is placed in a surrounding medium of water, the circular EFCs of the PC can be tuned to match the circular EFCs of the outside, homogeneous medium ($\rho_{water} = 1.0$ kg/m^3, $c_{t,water} = 0$ m/s, and $c_{l,water} = 1490$ m/s). This configuration has been utilized in previous work on negative refraction and focusing with phononic structures, because at 550 kHz, the PC has a refractive index of –1.[5] A line is superposed on the band structure in Fig. 10 to describe the non-dispersive behavior of water. This line intersects the band structure of the PC at 550 kHz and the condition for a refractive index of –1 is affirmed. The EFCs for the steel/methanol PC are illustrated in Figs. 11(a), 11(b), and 11(c) along with the EFCs for acoustic waves in water (left and right hand circles) at frequencies 530, 550, and 570 kHz, respectively. As frequency increases, the size of the circular EFCs in the PC decreases. This is because of the negative slope in the band structure at these frequencies. Alongside Figs. 11(a), 11(b), and 11(c) are schematic illustrations of two waves impinging upon the PC. Two incident beams are directed at the PC face and enter the crystal at precisely the same point. This point of entry coincides with the horizontal,

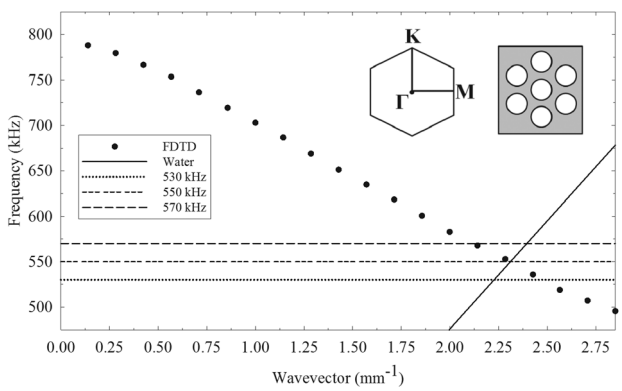

FIG. 10. The band structure along the ΓM direction for the infinite, periodic steel/methanol PC generated by the FDTD method. In the range of 530–570 kHz, we observe a passing band with negative group velocity. In this operating frequency range, circular EFCs can be realized where the wave and group velocity vectors of excited Bloch modes are collinear and anti-parallel.

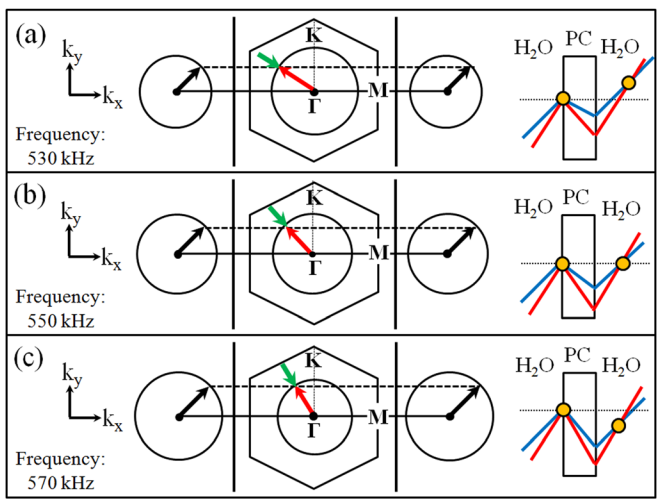

FIG. 11. (Color online) *k*-space schematic for steel/methanol PC immersed in a surrounding environment of water (a, b, and c left-hand illustrations) and rendering of two acoustic waves in water impinging upon the PC (a, b, and c right-hand illustrations). In (a, left), the radius of the circular EFC in the PC (center circle) is larger than the radii of the circular EFCs in water (left- and right-hand circles). The incidence angle is greater in magnitude than the refracted angle. In (a, right), the two impinging acoustic waves will negatively refract in the PC by values smaller than their incidence angles. Accordingly, the beams will intersect on the exit side of the PC at a location above their point of entry (dotted line). In (b, left), the radius of the circular EFC in the PC equals the radii of the circular EFCs in water. The incidence angle value is equal in magnitude to the refracted angle value. In (b, right), the two impinging acoustic waves will negatively refract in the PC by values equal to their incidence angles. Accordingly, the beams will intersect on the exit side of the PC precisely at a level consistent with their point of entry (dotted line). In (c, left), the radius of the circular EFC in the PC is smaller than the radii of the circular EFCs in water. The incidence angle is smaller in magnitude than the refracted angle. In (c, right), the two impinging acoustic waves will negatively refract in the PC by values greater than their incidence angles. Accordingly, the beams will intersect on the exit side of the PC at a location below their point of entry (dotted line). Bloch wave vectors in the PC k-space originate from the Gamma point; group velocity vectors are collinear and anti-parallel to excited Bloch modes.

dotted line drawn in the schematic illustration. At 530 kHz, the EFC in the PC is larger than the EFC of the outside, homogeneous medium. Accordingly, for both inputs, the degree of refraction inside the PC is smaller than the incidence angle. In this case, the beams will intersect at a point on the backside of the PC that is above the dotted line. At 550 kHz, the EFC in the PC matches the size of the EFC of the surrounding medium. For both input beams, the degree of refraction in the PC is equal to the incidence angle. In this case, on the exit side of the crystal, the beams intersect precisely at the dotted line. At 570 kHz, the EFC in the PC is smaller than the EFC in water and, for both input beams, the degree of refraction in the PC is greater than the incidence angle. Accordingly, this causes the beams to intersect at a point below the dotted line. The point of beam intersection on the exit side of the PC is utilized later for characterizing the total relative phase shift between the beams.

To detail the propagation of two arbitrary input waves to the system in the frequency range 530–570 kHz, we use Fig. 12. In this illustration, the radii of the circular EFC in the PC and the circular EFC in water are arbitrary. Two impinging incident waves with wave vectors $\overrightarrow{k_1}$ and $\overrightarrow{k_2}$ (incidence angles θ_1 and θ_2) are directed at the PC face,

$$\overrightarrow{k_1} = R_o \cos(\theta_1) i + R_o \sin(\theta_1) j,$$

$$\overrightarrow{k_2} = R_o \cos(\theta_2) i + R_o \sin(\theta_2) j.$$

R_o is the radius of the EFC in water (units of wave number: radians per length). These impinging waves are negatively refracted by a value consistent with the following relationship:

$$\theta' = sin^{-1}\left(\frac{R_o \sin(\theta)}{R_{pc}}\right).$$

The parallel components of these impinging wave vectors excite Bloch waves $\overrightarrow{k_1'}$ and $\overrightarrow{k_2'}$ within the k-space of the PC,

$$\overrightarrow{k_1'} = -R_{pc} \cos(\theta_1') i + R_o \sin(\theta_1) j,$$

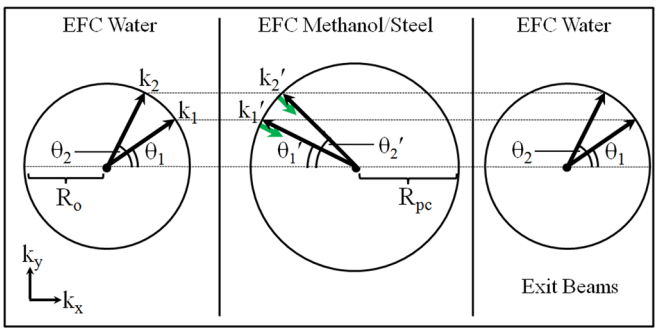

FIG. 12. (Color online) Two impinging incident waves with wave vectors $\overrightarrow{k_1}$ and $\overrightarrow{k_2}$ (incidence angles θ_1 and θ_2) are directed at the steel/methanol PC and excite Bloch waves $\overrightarrow{k_1'}$ and $\overrightarrow{k_2'}$ within the k-space of the PC. The incident waves are negatively refracted in the PC according to angles θ_1', and θ_2', and travel in a direction consistent with the group velocity vectors (arrows anti-parallel to the excited Bloch wave vectors). The radius of the circular EFCs in water and the PC are R_o and R_{pc}, respectively.

$$\overrightarrow{k_2'} = -R_{pc} \cos(\theta_2') i + R_o \sin(\theta_2) j.$$

R_{pc} is the radius of the circular EFC in the PC (units of wave number: radians per length). The directions of propagation for the refracted beams are written as follows:

The incident beam $\overrightarrow{k_1}$ is refracted by an angle θ_1' and travels a path in the PC consistent with

$$\overrightarrow{r_1} = Li - L\tan(\theta_1').$$

The incident beam $\overrightarrow{k_2}$ is refracted by an angle θ_2' and travels a path that coincides with

$$\overrightarrow{r_2} = Li - L\tan(\theta_2') j.$$

L, again, is the PC thickness. In this scheme, with the orientation of the triangular lattice (ΓM direction), L is given in terms of layers of cylinders instead of lattice parameters. Equation (14) details phase information for a plane wave with wave vector $\overrightarrow{k_1'}$ traveling a path consistent with $\overrightarrow{r_1}$,

$$\varphi_1 = \overrightarrow{k_1'} \cdot \overrightarrow{r_1} = L\{-R_{pc} \cos(\theta_1') - R_o \sin(\theta_1) tan(\theta_1')\}. \quad (14)$$

Similarly, for a plane wave with wave vector $\overrightarrow{k_2'}$ traveling a path consistent with $\overrightarrow{r_2}$, we have

$$\varphi_2 = \overrightarrow{k_2'} \cdot \overrightarrow{r_2} = L\{-R_{pc} \cos(\theta_2') - R_o \sin(\theta_2) tan(\theta_2')\}. \quad (15)$$

After propagation through the PC, the phase-difference developed between Bloch waves with wave vectors $\overrightarrow{k_1'}$ and $\overrightarrow{k_2'}$ is described with Eq. (16),

$$\varphi_{12} = \overrightarrow{k_1'} \cdot \overrightarrow{r_1} - \overrightarrow{k_2'} \cdot \overrightarrow{r_2},$$
$$\varphi_{12} = LR_{pc}\{\cos(\theta_2') - \cos(\theta_1')\} + LR_o\{\sin(\theta_2)\tan(\theta_2') - \sin(\theta_1)\tan(\theta_1')\}. \quad (16)$$

Equation (16) is the phase shift developed between two incident beams strictly due to the PC thickness. The results of this equation are shown in Figs. 13(a), 13(b), and 13(c) (as φ/L) for operating frequencies of 530, 550, and 570 kHz, respectively. In these figures, considerable phase-shifts can result within the confines of the PC. The developed difference in phase between waves in this instance is only attributed to waves of the same phase velocity traveling different path lengths. The maxima or minima on these surfaces show that greater phase differences result when the difference in the length of the refracted beam paths is large.

To stay consistent with the method used to evaluate the PVC/air system, we must consider the total relative phase shift between the waves — the phase difference developed from the point where the beams first enter the crystal to the point where the beams intersect on the exit side of the PC. With this notion, an additional component needs to be added onto the information contained in Figs. 13(a), 13(b), and 13(c): the relative phase contribution coming from the point where the beams exit the crystal to the point where they intersect on the exit side of the PC. This component is a

consideration of different path lengths in non-dispersive media. In observing the schematic illustrations in Figs. 11(a), 11(b), and 11(c), the paths of travel for the beams on the exit side of the PC can be understood. Like the PVC/air system, for each set of incident waves to the crystal, the additional phase value on the exit side of the PC is determined from comparing path lengths calculated from the angles at which the two beams leave the PC and knowledge of where the beams exit from the backside of the crystal. These additional calculations are added onto the information in Figs. 13(a), 13(b), and 13(c) for a crystal with thickness $L = 46$ layers (stacked in the ΓM direction). This specific crystal thickness is used to compare the steel/methanol system with the PVC/air system; the PVC/Air system could achieve a 2π shift in relative phase with this L-value. The new plots for total phase shift are presented in Figs. 14(a), 14(b), and 14(c). Total phase shift refers to the phase difference developed from the point where the beams first enter the crystal to the point where the beams intersect in water on the exit side of the PC. Attention is immediately directed at Fig. 14(b). At 550 kHz, the condition where the PC has a refractive index of –1, the total phase shift resulting between any two incident beams is zero. This can be explained because, in this instance, the radius of the EFC in water equals the radius of the EFC in the PC. Accordingly, the angle of incidence of an incoming beam always equals negative the angle of the refracted beam (Fig. 11(b)). Therefore, from Eq. (16), for any two impinging waves at 550 kHz, the developed difference in relative phase due to a PC of thickness L is

$$\varphi_{12} = \frac{-RL}{\cos(\theta_1)} + \frac{RL}{\cos(\theta_2)}. \tag{17}$$

R corresponds to the radius of the matching EFCs in water and the PC. On the exit side of the PC, the wave vectors detailed in water are described as follows:

$$\overrightarrow{k_1} = R\cos(\theta_1)i + R\sin(\theta_1)j,$$
$$\overrightarrow{k_2} = R\cos(\theta_2)i + R\sin(\theta_2)j.$$

Figure 12 can be used to visualize this result. Additionally, because of the matching EFCs in water and the PC, the paths of travel in the exit medium for the two beams are written as

$$\overrightarrow{r_1} = Li + Ltan(\theta_1)j,$$
$$\overrightarrow{r_2} = Li + Ltan(\theta_2)j.$$

The developed difference in relative phase on the exit side of the PC is shown in Eq. (18),

$$\varphi_{12} = \overrightarrow{k_1}\cdot\overrightarrow{r_1} - \overrightarrow{k_2}\cdot\overrightarrow{r_2}, \quad \varphi_{12} = \frac{RL}{\cos(\theta_1)} - \frac{RL}{\cos(\theta_2)}. \tag{18}$$

The summation of the relative phase shift between the beams inside the PC (Eq. (17)) with the relative phase shift between the beams on the exit side of the PC (Eq. (18)) yields a value of zero; therefore, the results seen in Fig. 14(b) are confirmed. For Figs. 14(a) (530 kHz) and 14(c) (570 kHz), a non-zero value in total relative phase shift does result between the input beams. This value, however, is comparably smaller to that observed in the PVC/air system for the same number of layers ($L = 46$). In the PVC/air system, a

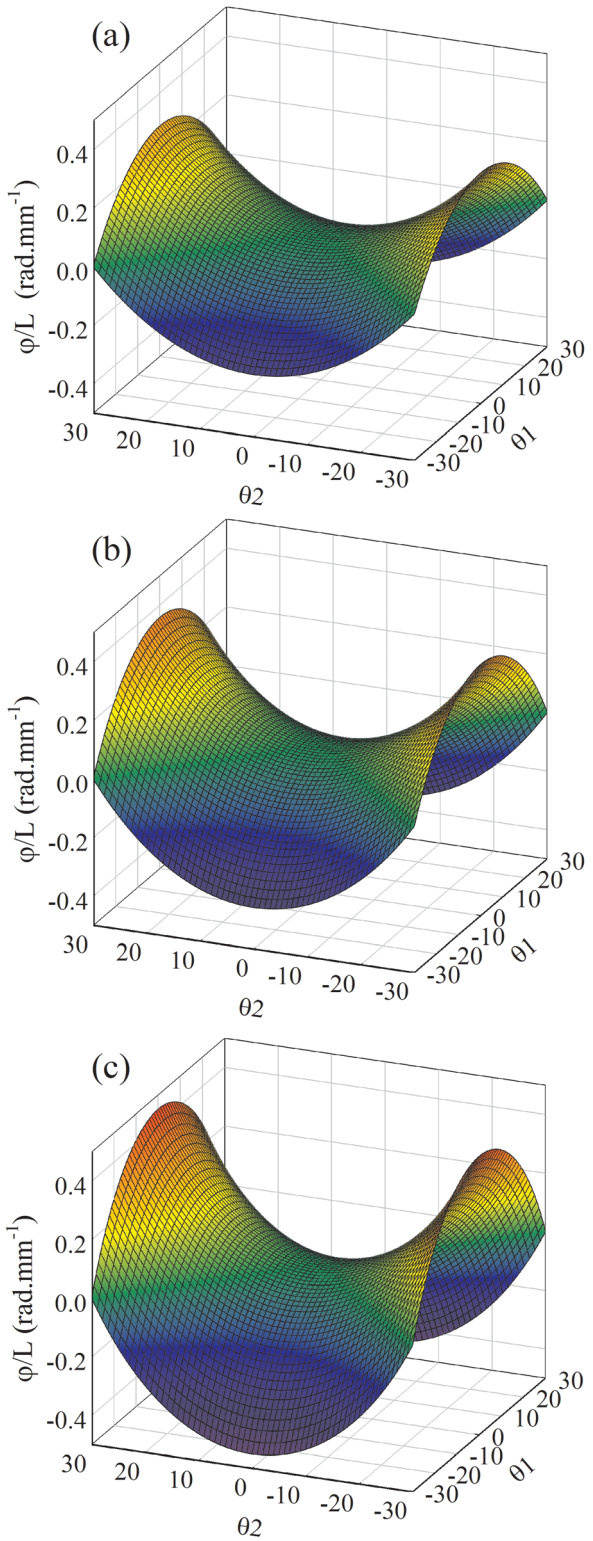

FIG. 13. (Color online) The developed phase difference between impinging beams with incident angles θ_1 and θ_2 strictly due to the PC thickness (L) for (a) 530 kHz, (b) 550 kHz, and (c) 570 kHz. The developed difference in phase between waves is attributed to waves of the same phase velocity traveling different path lengths. The maxima or minima on these surfaces show that greater phase differences result when the difference in the length of the refracted beam paths is large.

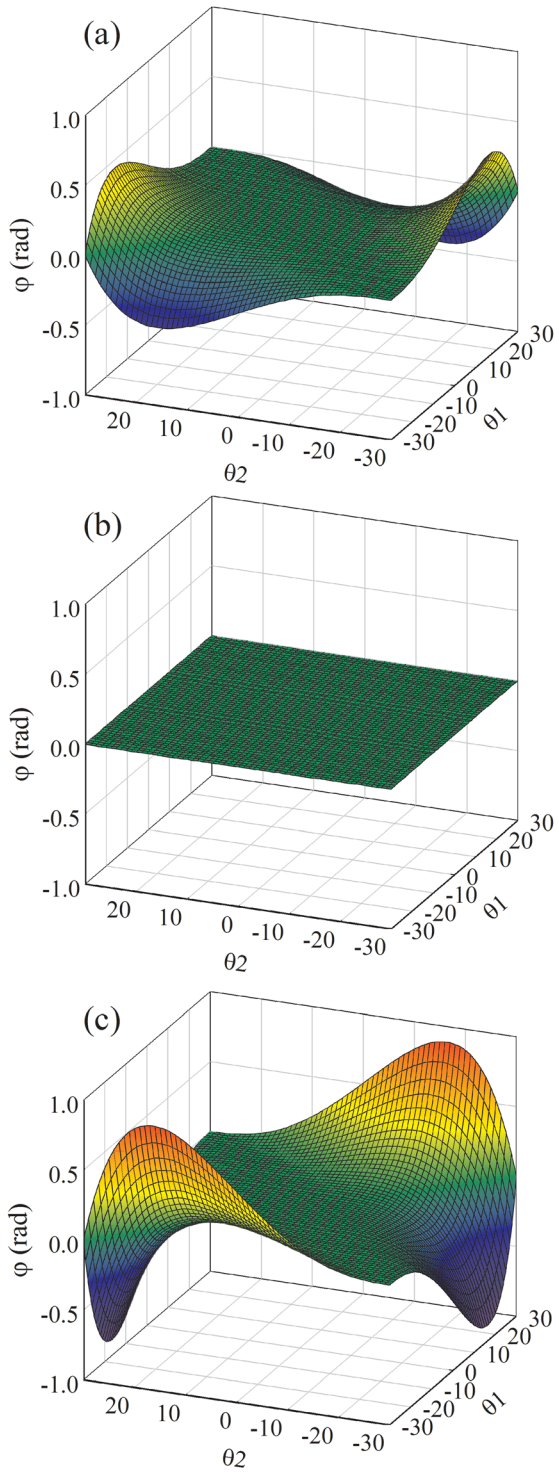

FIG. 14. (Color online) Total phase shift between two impinging acoustic waves for the methanol/steel PC immersed in water at (a) 530 kHz, (b) 550 kHz, and (c) 570 kHz. Total phase shift refers to the phase difference developed from the point where the beams first enter the PC to the point where the beams intersect on the exit side of the PC. In (b), because the radius of the PC circular EFC perfectly matches the radius of the EFC for water, a relative phase difference of zero results between all acoustic wave inputs.

relative phase shift of 2π was resolved between two input beams. The maximum value in total relative phase shift that can be seen in the steel/methanol system with $L=46$ is approximately 0.45 rads for 530 kHz and 0.8 rads for 570 kHz. To achieve a relative phase shift of 2π in the steel/methanol system at the operating frequencies of 530 and 570 kHz, the crystal thickness value ($L=46$ layers) needs to be multiplied by approximately 14 and 7, respectively. Crystal thicknesses such as these are extremely impractical systems to use in experimental work (energy losses and attenuation) and are exceedingly difficult to model numerically (FDTD computation time would be prohibitive). It is apparent that the steel/methanol system, in this range of operating frequencies, is not ideal for initiating phase differences between acoustic wave pairs. This conclusion comes from the fact that the wave and group velocity vectors in this PC are collinear and anti-parallel. Because the waves travel at the same phase velocity inside the PC (and outside the PC in the homogeneous medium), the only contributing element to developing a phase difference with this system is path length. This does not relate with significant values in phase differences.

V. CONCLUSIONS

We have theoretically investigated the phase properties of two PCs by constructing analytical models based on their respective band structures and EFCs. The PVC/air system features square-like EFCs near an operating frequency of 13.5 kHz and, because these contours are not centered on the Gamma point, the wave and group velocity vectors in the PC are non-collinear. The steel/methanol system, at the considered operating frequencies, offers circular EFCs centered on the gamma point, which allows for collinear and anti-parallel wave and group velocity vectors. In comparing these models, we have shown that the PVC/air system achieves substantial relative phase shifts between waves propagating through the system. This function is enabled by having excited Bloch modes in the PC with different phase velocities that propagate along different paths. Specifically, phase control in the PVC/air system arises from non-collinear wave and group velocity vectors in the PC. The steel/methanol system does not achieve substantial relative phase shifts between acoustic wave inputs, because all excited Bloch modes travel at one, specific phase velocity. To practically utilize the phase-space functionalities of two-dimensional PC systems, crystals with band structures and EFCs showing non-collinear wave and group velocity vectors should be used.

ACKNOWLEDGMENTS

We gratefully acknowledge support from NSF grant #0924103.

[1]J. O. Vasseur, P. Deymier, B. Chenni, B. Djafari-Rouhani, L. Dobrzynski, and D. Prevost, Phys. Rev. Lett. **86**(14), 3012 (2001).
[2]A. Khelif, P. A. Deymier, B. Djafari-Rouhani, J. Vasseur, and L. Dobrzynski, J. Appl. Phys. **94**, 1308 (2003).
[3]J. O. Vasseur, P. Deymier, B. Djafari-Rouhani, Y. Pennec, and A. Hladky-Hennion, Phys. Rev. B **77**(8), 85415 (2008).
[4]N. Fang, D. Xi, J. Xu, M. Ambati, W. Srituravanich, C. Sun, and X. Zhang, Nature Mater. **5**(6), 452 (2006).
[5]A. Sukhovich, B. Merheb, K. Muralidharan, J. O. Vasseur, Y. Pennec, P. A. Deymier, and J. Page, Phys. Rev. Lett. **102**, 154301 (2009).
[6]V. Espinosa, V. J. Sanchez-Morcillo, K. Staliunas, I. Perez-Arjona, and J. Redondo, Phys. Rev. B **76**, 140302 (2007).
[7]I. Perez-Arjona, V. J. Sanchez-Morcillo, J. Redondo, V. Espinosa, and K. Staliunas, Phys. Rev. B **75**, 014304 (2007).
[8]M. Kafesaki, M. M. Sigalas, and N. García, Physica B **296**(1–3), 190 (2001).
[9]B. Liang, X. S. Guo, J. Tu, D. Zhang, and J. C. Cheng, Nature Mater. **9**, 989 (2010).

[10]J. F. Robillard, O. B. Matar, J. O. Vasseur, P. A. Deymier, M. Stippinger, A. C. Hladky, Hennion, Y. Pennec, and B. Djafari-Rouhani, Appl. Phys. Lett. **95**, 124104 (2009).
[11]N. Swinteck, J.-F., Robillard, S. Bringuier, J. Bucay, K. Muralidharan, J. O. Vasseur, K. Runge and P. A. Deymier, Appl. Phys. Lett. **98**, 103508 (2011).
[12]M. S. Kushwaha, B. Djafari-Rouhani, L. Dobrzynski, and J. O. Vasseur, Eur. Phys. J. B **3**, 155 (1998).
[13]D. Garcia-Pablos, M. Sigalas, F. R. Montero de Espinosa, M. Torres, M. Kafesaki, and N. Garcia, Phys. Rev. Lett. **84**, 4349 (2000).
[14]T. Miyashita and C. Inoue, Jpn. J. Appl. Phys., Part 1 **40**, 3488 (2001).
[15]Lambin, A. Khelif, J. O. Vasseur, L. Dobrynski, and B. Djafari-Rouhani, Phys. Rev. E **63**, 066605 (2001).
[16]M. Sigalas and N. Garcia, J. Appl. Phys. **87**, 3122 (2000).
[17]M. Torres, F. R. Montero de Espinosa, and J. L. Aragon, Phys. Rev. Lett. **86**, 4282 (2001).
[18]G. Mur, IEEE Trans. Electromagn. Compat. **EMC-23**, 377 (1981).
[19]Y. Tanaka, Y. Tomoyasu, and S. Tamura, Phys. Rev. B **62**, 7387 (2000).